University of Nebraska - Lincoln
DigitalCommons@University of Nebraska - Lincoln

Kenneth Bloom Publications | Research Papers in Physics and Astronomy

7-10-2007

Measurement of the shape of the boson rapidity distribution for $p\bar{p} \to Z/\gamma^* \to e^+e^- + X$ events produced at $\sqrt{s}$ of 1.96 TeV

V.M. Abazov
Joint Institute for Nuclear Research, Dubna, Russia

Kenneth A. Bloom
University of Nebraska - Lincoln, kbloom2@unl.edu

Gregory R. Snow
University of Nebraska-Lincoln, gsnow1@unl.edu

D0 Collaboration

Follow this and additional works at: http://digitalcommons.unl.edu/physicsbloom

 Part of the Physics Commons

Abazov, V.M.; Bloom, Kenneth A.; Snow, Gregory R.; and Collaboration, D0, "Measurement of the shape of the boson rapidity distribution for $p\bar{p} \to Z/\gamma^* \to e^+e^- + X$ events produced at $\sqrt{s}$ of 1.96 TeV" (2007). *Kenneth Bloom Publications*. 215.
http://digitalcommons.unl.edu/physicsbloom/215

This Article is brought to you for free and open access by the Research Papers in Physics and Astronomy at DigitalCommons@University of Nebraska - Lincoln. It has been accepted for inclusion in Kenneth Bloom Publications by an authorized administrator of DigitalCommons@University of Nebraska - Lincoln.

Measurement of the shape of the boson rapidity distribution for $p\bar{p} \to Z/\gamma^* \to e^+e^- + X$ events produced at $\sqrt{s}$ of 1.96 TeV

V. M. Abazov,[35] B. Abbott,[75] M. Abolins,[65] B. S. Acharya,[28] M. Adams,[51] T. Adams,[49] E. Aguilo,[5] S. H. Ahn,[30] M. Ahsan,[59] G. D. Alexeev,[35] G. Alkhazov,[39] A. Alton,[64,*] G. Alverson,[63] G. A. Alves,[2] M. Anastasoaie,[34] L. S. Ancu,[34] T. Andeen,[53] S. Anderson,[45] B. Andrieu,[16] M. S. Anzelc,[53] Y. Arnoud,[13] M. Arov,[52] A. Askew,[49] B. Åsman,[40] A. C. S. Assis Jesus,[3] O. Atramentov,[49] C. Autermann,[20] C. Avila,[7] C. Ay,[23] F. Badaud,[12] A. Baden,[61] L. Bagby,[52] B. Baldin,[50] D. V. Bandurin,[59] P. Banerjee,[28] S. Banerjee,[28] E. Barberis,[63] A.-F. Barfuss,[14] P. Bargassa,[80] P. Baringer,[58] J. Barreto,[2] J. F. Bartlett,[50] U. Bassler,[16] D. Bauer,[43] S. Beale,[5] A. Bean,[58] M. Begalli,[3] M. Begel,[71] C. Belanger-Champagne,[40] L. Bellantoni,[50] A. Bellavance,[67] J. A. Benitez,[65] S. B. Beri,[26] G. Bernardi,[16] R. Bernhard,[22] L. Berntzon,[14] I. Bertram,[42] M. Besançon,[17] R. Beuselinck,[43] V. A. Bezzubov,[38] P. C. Bhat,[50] V. Bhatnagar,[26] M. Binder,[24] C. Biscarat,[19] G. Blazey,[52] F. Blekman,[43] S. Blessing,[49] D. Bloch,[18] K. Bloom,[67] A. Boehnlein,[50] D. Boline,[62] T. A. Bolton,[59] G. Borissov,[42] K. Bos,[33] T. Bose,[77] A. Brandt,[78] R. Brock,[65] G. Brooijmans,[70] A. Bross,[50] D. Brown,[78] N. J. Buchanan,[49] D. Buchholz,[53] M. Buehler,[81] V. Buescher,[21] S. Burdin,[50] S. Burke,[45] T. H. Burnett,[82] E. Busato,[16] C. P. Buszello,[43] J. M. Butler,[62] P. Calfayan,[24] S. Calvet,[14] J. Cammin,[71] S. Caron,[33] W. Carvalho,[3] B. C. K. Casey,[77] N. M. Cason,[55] H. Castilla-Valdez,[32] S. Chakrabarti,[17] D. Chakraborty,[52] K. Chan,[5] K. M. Chan,[71] A. Chandra,[48] F. Charles,[18] E. Cheu,[45] F. Chevallier,[13] D. K. Cho,[62] S. Choi,[31] B. Choudhary,[27] L. Christofek,[77] T. Christoudias,[43] S. Cihangir,[50] D. Claes,[67] B. Clément,[18] C. Clément,[40] Y. Coadou,[5] M. Cooke,[80] W. E. Cooper,[50] M. Corcoran,[80] F. Couderc,[17] M.-C. Cousinou,[14] S. Crépé-Renaudin,[13] D. Cutts,[77] M. Ćwiok,[29] H. da Motta,[2] A. Das,[62] G. Davies,[43] K. De,[78] P. de Jong,[33] S. J. de Jong,[34] E. De La Cruz-Burelo,[64] C. De Oliveira Martins,[3] J. D. Degenhardt,[64] F. Déliot,[17] M. Demarteau,[50] R. Demina,[71] D. Denisov,[50] S. P. Denisov,[38] S. Desai,[50] H. T. Diehl,[50] M. Diesburg,[50] A. Dominguez,[67] H. Dong,[72] L. V. Dudko,[37] L. Duflot,[15] S. R. Dugad,[28] D. Duggan,[49] A. Duperrin,[14] J. Dyer,[65] A. Dyshkant,[52] M. Eads,[67] D. Edmunds,[65] J. Ellison,[48] V. D. Elvira,[50] Y. Enari,[77] S. Eno,[61] P. Ermolov,[37] H. Evans,[54] A. Evdokimov,[36] V. N. Evdokimov,[38] A. V. Ferapontov,[59] T. Ferbel,[71] F. Fiedler,[24] F. Filthaut,[34] W. Fisher,[50] H. E. Fisk,[50] M. Ford,[44] M. Fortner,[52] H. Fox,[22] S. Fu,[50] S. Fuess,[50] T. Gadfort,[82] C. F. Galea,[34] E. Gallas,[50] E. Galyaev,[55] C. Garcia,[71] A. Garcia-Bellido,[82] V. Gavrilov,[36] P. Gay,[12] W. Geist,[18] D. Gelé,[18] C. E. Gerber,[51] Y. Gershtein,[49] D. Gillberg,[5] G. Ginther,[71] N. Gollub,[40] B. Gómez,[7] A. Goussiou,[55] P. D. Grannis,[72] H. Greenlee,[50] Z. D. Greenwood,[60] E. M. Gregores,[4] G. Grenier,[19] Ph. Gris,[12] J.-F. Grivaz,[15] A. Grohsjean,[24] S. Grünendahl,[50] M. W. Grünewald,[29] F. Guo,[72] J. Guo,[72] G. Gutierrez,[50] P. Gutierrez,[75] A. Haas,[70] N. J. Hadley,[61] P. Haefner,[24] S. Hagopian,[49] J. Haley,[68] I. Hall,[75] R. E. Hall,[47] L. Han,[6] K. Hanagaki,[50] P. Hansson,[40] K. Harder,[44] A. Harel,[71] R. Harrington,[63] J. M. Hauptman,[57] R. Hauser,[65] J. Hays,[43] T. Hebbeker,[20] D. Hedin,[52] J. G. Hegeman,[33] J. M. Heinmiller,[51] A. P. Heinson,[48] U. Heintz,[62] C. Hensel,[58] K. Herner,[72] G. Hesketh,[63] M. D. Hildreth,[55] R. Hirosky,[81] J. D. Hobbs,[72] B. Hoeneisen,[11] H. Hoeth,[25] M. Hohlfeld,[15] S. J. Hong,[30] R. Hooper,[77] P. Houben,[33] Y. Hu,[72] Z. Hubacek,[9] V. Hynek,[8] I. Iashvili,[69] R. Illingworth,[50] A. S. Ito,[50] S. Jabeen,[62] M. Jaffré,[15] S. Jain,[75] K. Jakobs,[22] C. Jarvis,[61] R. Jesik,[43] K. Johns,[45] C. Johnson,[70] M. Johnson,[50] A. Jonckheere,[50] P. Jonsson,[43] A. Juste,[50] D. Käfer,[20] S. Kahn,[73] E. Kajfasz,[14] A. M. Kalinin,[35] J. M. Kalk,[60] J. R. Kalk,[65] S. Kappler,[20] D. Karmanov,[37] J. Kasper,[62] P. Kasper,[50] I. Katsanos,[70] D. Kau,[49] R. Kaur,[26] V. Kaushik,[78] R. Kehoe,[79] S. Kermiche,[14] N. Khalatyan,[38] A. Khanov,[76] A. Kharchilava,[69] Y. M. Kharzheev,[35] D. Khatidze,[70] H. Kim,[31] T. J. Kim,[30] M. H. Kirby,[34] B. Klima,[50] J. M. Kohli,[26] J.-P. Konrath,[22] M. Kopal,[75] V. M. Korablev,[38] J. Kotcher,[73] B. Kothari,[70] A. Koubarovsky,[37] A. V. Kozelov,[38] D. Krop,[54] A. Kryemadhi,[81] T. Kuhl,[23] A. Kumar,[69] S. Kunori,[61] A. Kupco,[10] T. Kurča,[19] J. Kvita,[8] D. Lam,[55] S. Lammers,[70] G. Landsberg,[77] J. Lazoflores,[49] P. Lebrun,[19] W. M. Lee,[50] A. Leflat,[37] F. Lehner,[41] V. Lesne,[12] J. Leveque,[45] P. Lewis,[43] J. Li,[78] L. Li,[48] Q. Z. Li,[50] S. M. Lietti,[4] J. G. R. Lima,[52] D. Lincoln,[50] J. Linnemann,[65] V. V. Lipaev,[38] R. Lipton,[50] Z. Liu,[5] L. Lobo,[43] A. Lobodenko,[39] M. Lokajicek,[10] A. Lounis,[18] P. Love,[42] H. J. Lubatti,[82] M. Lynker,[55] A. L. Lyon,[50] A. K. A. Maciel,[2] R. J. Madaras,[46] P. Mättig,[25] C. Magass,[20] A. Magerkurth,[64] N. Makovec,[15] P. K. Mal,[55] H. B. Malbouisson,[3] S. Malik,[67] V. L. Malyshev,[35] J. Mans,[61] H. S. Mao,[50] Y. Maravin,[59] B. Martin,[13] R. McCarthy,[72] A. Melnitchouk,[66] A. Mendes,[14] L. Mendoza,[7] P. G. Mercadante,[4] M. Merkin,[37] K. W. Merritt,[50] A. Meyer,[20] J. Meyer,[21] M. Michaut,[17] H. Miettinen,[80] T. Millet,[19] J. Mitrevski,[70] J. Molina,[3] R. K. Mommsen,[44] N. K. Mondal,[28] J. Monk,[44] R. W. Moore,[5] T. Moulik,[58] G. S. Muanza,[19] M. Mulders,[50] M. Mulhearn,[70] O. Mundal,[21] L. Mundim,[3] E. Nagy,[14] M. Naimuddin,[50] M. Narain,[77] N. A. Naumann,[34] H. A. Neal,[64] J. P. Negret,[7] P. Neustroev,[39] H. Nilsen,[22] C. Noeding,[22] A. Nomerotski,[50] S. F. Novaes,[4] T. Nunnemann,[24] V. O'Dell,[50] D. C. O'Neil,[5] G. Obrant,[39] C. Ochando,[15] V. Oguri,[3] N. Oliveira,[3] D. Onoprienko,[59] N. Oshima,[50] J. Osta,[55] R. Otec,[9] G. J. Otero y Garzón,[51] M. Owen,[44] P. Padley,[80] M. Pangilinan,[77] N. Parashar,[56] S.-J. Park,[71] S. K. Park,[30] J. Parsons,[70] R. Partridge,[77] N. Parua,[72]

 © 2007 The American Physical Society

A. Patwa,[73] G. Pawloski,[80] P. M. Perea,[48] K. Peters,[44] Y. Peters,[25] P. Pétroff,[15] M. Petteni,[43] R. Piegaia,[1] J. Piper,[65] M.-A. Pleier,[21] P. L. M. Podesta-Lerma,[32,†] V. M. Podstavkov,[50] Y. Pogorelov,[55] M.-E. Pol,[2] A. Pompoš,[75] B. G. Pope,[65] A. V. Popov,[38] C. Potter,[5] W. L. Prado da Silva,[3] H. B. Prosper,[49] S. Protopopescu,[73] J. Qian,[64] A. Quadt,[21] B. Quinn,[66] M. S. Rangel,[2] K. J. Rani,[28] K. Ranjan,[27] P. N. Ratoff,[42] P. Renkel,[79] S. Reucroft,[63] M. Rijssenbeek,[72] I. Ripp-Baudot,[18] F. Rizatdinova,[76] S. Robinson,[43] R. F. Rodrigues,[3] C. Royon,[17] P. Rubinov,[50] R. Ruchti,[55] G. Sajot,[13] A. Sánchez-Hernández,[32] M. P. Sanders,[16] A. Santoro,[3] G. Savage,[50] L. Sawyer,[60] T. Scanlon,[43] D. Schaile,[24] R. D. Schamberger,[72] Y. Scheglov,[39] H. Schellman,[53] P. Schieferdecker,[24] C. Schmitt,[25] C. Schwanenberger,[44] A. Schwartzman,[68] R. Schwienhorst,[65] J. Sekaric,[49] S. Sengupta,[49] H. Severini,[75] E. Shabalina,[51] M. Shamim,[59] V. Shary,[17] A. A. Shchukin,[38] R. K. Shivpuri,[27] D. Shpakov,[50] V. Siccardi,[18] R. A. Sidwell,[59] V. Simak,[9] V. Sirotenko,[50] P. Skubic,[75] P. Slattery,[71] D. Smirnov,[55] R. P. Smith,[50] G. R. Snow,[67] J. Snow,[74] S. Snyder,[73] S. Söldner-Rembold,[44] L. Sonnenschein,[16] A. Sopczak,[42] M. Sosebee,[78] K. Soustruznik,[8] M. Souza,[2] B. Spurlock,[78] J. Stark,[13] J. Steele,[60] V. Stolin,[36] D. A. Stoyanova,[38] J. Strandberg,[64] S. Strandberg,[40] M. A. Strang,[69] M. Strauss,[75] R. Ströhmer,[24] D. Strom,[53] M. Strovink,[46] L. Stutte,[50] S. Sumowidagdo,[49] P. Svoisky,[55] A. Sznajder,[3] M. Talby,[14] P. Tamburello,[45] A. Tanasijczuk,[1] W. Taylor,[5] P. Telford,[44] J. Temple,[45] B. Tiller,[24] F. Tissandier,[12] M. Titov,[22] V. V. Tokmenin,[35] M. Tomoto,[50] T. Toole,[61] I. Torchiani,[22] T. Trefzger,[23] S. Trincaz-Duvoid,[16] D. Tsybychev,[72] B. Tuchming,[17] C. Tully,[68] P. M. Tuts,[70] R. Unalan,[65] L. Uvarov,[39] S. Uvarov,[39] S. Uzunyan,[52] B. Vachon,[5] P. J. van den Berg,[33] B. van Eijk,[35] R. Van Kooten,[54] W. M. van Leeuwen,[33] N. Varelas,[51] E. W. Varnes,[45] A. Vartapetian,[78] I. A. Vasilyev,[38] M. Vaupel,[25] P. Verdier,[19] L. S. Vertogradov,[35] M. Verzocchi,[50] F. Villeneuve-Seguier,[43] P. Vint,[43] J.-R. Vlimant,[16] E. Von Toerne,[59] M. Voutilainen,[67,‡] M. Vreeswijk,[33] H. D. Wahl,[49] L. Wang,[61] M. H. L. S Wang,[50] J. Warchol,[55] G. Watts,[82] M. Wayne,[55] G. Weber,[23] M. Weber,[50] H. Weerts,[65] A. Wenger,[22,§] N. Wermes,[21] M. Wetstein,[61] A. White,[78] D. Wicke,[25] G. W. Wilson,[58] S. J. Wimpenny,[48] M. Wobisch,[50] D. R. Wood,[63] T. R. Wyatt,[44] Y. Xie,[77] S. Yacoob,[53] R. Yamada,[50] M. Yan,[61] T. Yasuda,[50] Y. A. Yatsunenko,[35] K. Yip,[73] H. D. Yoo,[77] S. W. Youn,[53] C. Yu,[13] J. Yu,[78] A. Yurkewicz,[72] A. Zatserklyaniy,[52] C. Zeitnitz,[25] D. Zhang,[50] T. Zhao,[82] B. Zhou,[64] J. Zhu,[72] M. Zielinski,[71] D. Zieminska,[54] A. Zieminski,[54] V. Zutshi,[52] and E. G. Zverev[37]

(D0 Collaboration)

[1]*Universidad de Buenos Aires, Buenos Aires, Argentina*
[2]*LAFEX, Centro Brasileiro de Pesquisas Físicas, Rio de Janeiro, Brazil*
[3]*Universidade do Estado do Rio de Janeiro, Rio de Janeiro, Brazil*
[4]*Instituto de Física Teórica, Universidade Estadual Paulista, São Paulo, Brazil*
[5]*University of Alberta, Edmonton, Alberta, Canada, Simon Fraser University, Burnaby, British Columbia, Canada, York University, Toronto, Ontario, Canada, and McGill University, Montreal, Quebec, Canada*
[6]*University of Science and Technology of China, Hefei, People's Republic of China*
[7]*Universidad de los Andes, Bogotá, Colombia*
[8]*Center for Particle Physics, Charles University, Prague, Czech Republic*
[9]*Czech Technical University, Prague, Czech Republic*
[10]*Center for Particle Physics, Institute of Physics, Academy of Sciences of the Czech Republic, Prague, Czech Republic*
[11]*Universidad San Francisco de Quito, Quito, Ecuador*
[12]*Laboratoire de Physique Corpusculaire, IN2P3-CNRS, Université Blaise Pascal, Clermont-Ferrand, France*
[13]*Laboratoire de Physique Subatomique et de Cosmologie, IN2P3-CNRS, Universite de Grenoble 1, Grenoble, France*
[14]*CPPM, IN2P3-CNRS, Université de la Méditerranée, Marseille, France*
[15]*Laboratoire de l'Accélérateur Linéaire, IN2P3-CNRS et Université Paris-Sud, Orsay, France*
[16]*LPNHE, IN2P3-CNRS, Universités Paris VI and VII, Paris, France*
[17]*DAPNIA/Service de Physique des Particules, CEA, Saclay, France*
[18]*IPHC, IN2P3-CNRS, Université Louis Pasteur, Strasbourg, France and Université de Haute Alsace, Mulhouse, France*
[19]*IPNL, Université Lyon 1, CNRS/IN2P3, Villeurbanne, France and Université de Lyon, Lyon, France*
[20]*III. Physikalisches Institut A, RWTH Aachen, Aachen, Germany*
[21]*Physikalisches Institut, Universität Bonn, Bonn, Germany*
[22]*Physikalisches Institut, Universität Freiburg, Freiburg, Germany*
[23]*Institut für Physik, Universität Mainz, Mainz, Germany*
[24]*Ludwig-Maximilians-Universität München, München, Germany*
[25]*Fachbereich Physik, University of Wuppertal, Wuppertal, Germany*
[26]*Panjab University, Chandigarh, India*
[27]*Delhi University, Delhi, India*
[28]*Tata Institute of Fundamental Research, Mumbai, India*

[29]University College Dublin, Dublin, Ireland
[30]Korea Detector Laboratory, Korea University, Seoul, Korea
[31]SungKyunKwan University, Suwon, Korea
[32]CINVESTAV, Mexico City, Mexico
[33]FOM-Institute NIKHEF and University of Amsterdam/NIKHEF, Amsterdam, The Netherlands
[34]Radboud University Nijmegen/NIKHEF, Nijmegen, The Netherlands
[35]Joint Institute for Nuclear Research, Dubna, Russia
[36]Institute for Theoretical and Experimental Physics, Moscow, Russia
[37]Moscow State University, Moscow, Russia
[38]Institute for High Energy Physics, Protvino, Russia
[39]Petersburg Nuclear Physics Institute, St. Petersburg, Russia
[40]Lund University, Lund, Sweden, Royal Institute of Technology and Stockholm University, Stockholm, Sweden, and Uppsala University, Uppsala, Sweden
[41]Physik Institut der Universität Zürich, Zürich, Switzerland
[42]Lancaster University, Lancaster, United Kingdom
[43]Imperial College, London, United Kingdom
[44]University of Manchester, Manchester, United Kingdom
[45]University of Arizona, Tucson, Arizona 85721, USA
[46]Lawrence Berkeley National Laboratory and University of California, Berkeley, California 94720, USA
[47]California State University, Fresno, California 93740, USA
[48]University of California, Riverside, California 92521, USA
[49]Florida State University, Tallahassee, Florida 32306, USA
[50]Fermi National Accelerator Laboratory, Batavia, Illinois 60510, USA
[51]University of Illinois at Chicago, Chicago, Illinois 60607, USA
[52]Northern Illinois University, DeKalb, Illinois 60115, USA
[53]Northwestern University, Evanston, Illinois 60208, USA
[54]Indiana University, Bloomington, Indiana 47405, USA
[55]University of Notre Dame, Notre Dame, Indiana 46556, USA
[56]Purdue University Calumet, Hammond, Indiana 46323, USA
[57]Iowa State University, Ames, Iowa 50011, USA
[58]University of Kansas, Lawrence, Kansas 66045, USA
[59]Kansas State University, Manhattan, Kansas 66506, USA
[60]Louisiana Tech University, Ruston, Louisiana 71272, USA
[61]University of Maryland, College Park, Maryland 20742, USA
[62]Boston University, Boston, Massachusetts 02215, USA
[63]Northeastern University, Boston, Massachusetts 02115, USA
[64]University of Michigan, Ann Arbor, Michigan 48109, USA
[65]Michigan State University, East Lansing, Michigan 48824, USA
[66]University of Mississippi, University, Mississippi 38677, USA
[67]University of Nebraska, Lincoln, Nebraska 68588, USA
[68]Princeton University, Princeton, New Jersey 08544, USA
[69]State University of New York, Buffalo, New York 14260, USA
[70]Columbia University, New York, New York 10027, USA
[71]University of Rochester, Rochester, New York 14627, USA
[72]State University of New York, Stony Brook, New York 11794, USA
[73]Brookhaven National Laboratory, Upton, New York 11973, USA
[74]Langston University, Langston, Oklahoma 73050, USA
[75]University of Oklahoma, Norman, Oklahoma 73019, USA
[76]Oklahoma State University, Stillwater, Oklahoma 74078, USA
[77]Brown University, Providence, Rhode Island 02912, USA
[78]University of Texas, Arlington, Texas 76019, USA
[79]Southern Methodist University, Dallas, Texas 75275, USA
[80]Rice University, Houston, Texas 77005, USA
[81]University of Virginia, Charlottesville, Virginia 22901, USA
[82]University of Washington, Seattle, Washington 98195, USA

[*]Visitor from Augustana College, Sioux Falls, SD, USA
[†]Visitor from ICN-UNAM, Mexico City, Mexico
[‡]Visitor from Helsinki Institute of Physics, Helsinki, Finland
[§]Visitor from Universität Zürich, Zürich, Switzerland

(Received 16 February 2007; published 16 July 2007)

We present a measurement of the shape of the boson rapidity distribution for $p\bar{p} \to Z/\gamma^* \to e^+e^- + X$ events at a center-of-mass energy of 1.96 TeV. The measurement is made for events with electron-positron mass $71 < M_{ee} < 111$ GeV and uses 0.4 fb^{-1} of data collected at the Fermilab Tevatron collider with the D0 detector. This measurement significantly reduces the uncertainties on the rapidity distribution in the forward region compared with previous measurements. Predictions of next-to-next-to-leading order (NNLO) QCD are found to agree well with the data over the full rapidity range.

DOI: 10.1103/PhysRevD.76.012003 PACS numbers: 13.60.Hb, 13.38.Dg, 13.85.Qk

I. INTRODUCTION

Kinematic distributions of Z/γ^* bosons produced in hadronic collisions provide a wealth of information on the fundamental interactions involved. At leading order, Z/γ^* bosons are produced at a proton/antiproton collider through the annihilation of a quark and an antiquark, with the partons in the proton and antiproton carrying momentum fractions x_1 and x_2, respectively. In turn, the rapidity of the boson, defined as $y = \frac{1}{2}\ln\frac{E+p_L}{E-p_L}$, where E is the energy of the boson and p_L is the component of its momentum along the beam direction, is directly related to the momentum fractions by

$$x_{1,2} = \frac{M_{Z/\gamma^*}}{\sqrt{s}} e^{\pm y}.$$

Here, M_{Z/γ^*} is the mass of the boson, and $\sqrt{s}$ is the center-of-mass energy. These kinematic distributions can be precisely reconstructed when the boson decays leptonically since the leptons can be accurately reconstructed, and the backgrounds to di-lepton final states are small. For low rapidity bosons, the leptons also have small pseudorapidity,

$$\eta = -\ln(\tan(\theta/2)),$$

where θ is the polar angle and is measured relative to the proton beam. High rapidity bosons are more likely to have initial states that have maximal $|x_1 - x_2|$ for the incident partons.

Although calculations are available at next-to-next-to-leading order in QCD (NNLO) for $\mathrm{d}\sigma/\mathrm{d}y$ for $p\bar{p} \to Z/\gamma^* \to \ell\bar{\ell} + X$ [1], few measurements of the differential cross section exist [2]. The forward rapidity region ($|y| > 1.5$) suffers from a smaller cross section and lower acceptance than the central rapidity region ($|y| < 1.5$), and has not yet been well tested. The forward region probes quarks with low x and high 4-momentum transfer squared Q^2 ($Q^2 \approx M_Z^2$) as well as quarks with very large x. Parton distribution functions (PDFs) in this regime are mainly determined by jet cross section data, which have very different experimental and theoretical systematic uncertainties than the electron measurements presented here, and by inclusive lepton scattering data taken mostly at much lower Q^2, which must be evolved to high momentum transfer scales using the DGLAP equations [3].

We measure the normalized differential cross section

$$\frac{1}{\sigma}\left(\frac{\mathrm{d}\sigma}{\mathrm{d}y}\right)_i = \frac{(\epsilon \times A)_{\mathrm{avg}}}{N^{\mathrm{obs}}_{\mathrm{total}} - N^{\mathrm{bg}}_{\mathrm{total}}} \frac{N^{\mathrm{obs}}_i - N^{\mathrm{bg}}_i}{\Delta_i(\epsilon \times A)_i},$$

where the index i indicates the boson rapidity bin. In the first term on the right-hand side, ϵ_{avg} is the average efficiency and A_{avg} is the average acceptance for kinematic and geometric cuts. $N^{\mathrm{obs}}_{\mathrm{total}}$ is the total number of candidate bosons, and $N^{\mathrm{bg}}_{\mathrm{total}}$ is the total number of background events in the sample. In the second term, ϵ_i, A_i, N^{obs}_i, and N^{bg}_i are the same as before, but determined in each bin i. Δ_i is the bin width. Dividing by the total number of events reduces many of the systematic uncertainties, particularly those due to luminosity.

The D0 detector [4] allows efficient detection of electrons [5] at the large pseudorapidities needed to study high rapidity Z/γ^* bosons. It has a central tracking system, consisting of a silicon microstrip tracker (SMT) and a central fiber tracker (CFT), both located within a 2 T superconducting solenoidal magnet, with designs optimized for tracking and vertexing [6] at pseudorapidities $|\eta_D| < 3$ and $|\eta_D| < 2.5$, respectively. The quantity η_D is η measured from the center of the detector. A liquid-argon and uranium calorimeter allows reconstruction of electrons, photons, jets, and missing transverse energy. The calorimeter is divided into a central section (CC) covering $|\eta_D| \lesssim 1.1$, and two end calorimeters (EC) that extend coverage to $|\eta_D| \approx 4.2$. Each calorimeter is housed in a separate cryostat [7]. An outer muon system, covering $|\eta_D| < 2$, consists of a layer of tracking detectors and scintillation trigger counters in front of 1.8 T iron toroids, followed by two similar layers after the toroids [8]. The luminosity is measured using plastic scintillator arrays placed in front of the EC cryostats. The trigger and data acquisition systems are designed to accommodate the high luminosities of Run II.

II. EVENT SELECTION

This measurement utilizes a data set of 0.4 fb^{-1} collected at the Fermilab Tevatron between 2002 and 2004. The data are from $p\bar{p}$ collisions at $\sqrt{s} = 1.96$ TeV. We consider candidate Z/γ^* events that decay into an electron-positron pair with a reconstructed invariant mass $71 <$

$M_{ee} < 111$ GeV. The range used is ± 20 GeV about the mass of the Z boson.

To optimize the acceptance for electrons at large η, two strategies are used. The first is to require only one of the electromagnetic clusters be matched to a reconstructed track. Requiring a track-matched electron helps to reduce background from jets misidentified as electrons, while removing the track requirement on the second electron extends the η coverage beyond that of the tracking system. The second strategy takes advantage of the length of the bunches containing the incident protons and antiprotons, which has a design length of 37 cm. For our data set, the z coordinate [9] of the primary interactions has a roughly Gaussian distribution with a rms ranging from 29 ± 2 cm to 24 ± 1 cm. The rms depends on run conditions and time. At large values of vertex $|z|$, some of the decay products will travel back through the detector towards smaller $|z|$ values. These particles pass through much of the active volume of the tracking system. Typically, these events have low background and have the highest boson rapidities.

Events are required to have passed a single electron trigger. To optimize the trigger efficiency, a collection of single electron trigger conditions are considered. D0 has a three level trigger system which is described in Ref. [4]. At level 1, typically 1 or 2 electromagnetic (EM) trigger towers are required to have transverse energy above p_T thresholds ranging from 5 to 15 GeV. The p_T of the candidate event is derived using the energy measured in the calorimeter; the polar angle is calculated assuming that the particle originated from the origin of the D0 coordinate system. The p_T is determined separately at each level of the trigger system. For the trigger conditions that have a level 2 requirement, the p_T of the candidate is calculated using a single clustering algorithm, and is required to be above thresholds of 12 to 15 GeV. At level 3 the full event data is analyzed using code that is very similar to the offline reconstruction. At this level, the shower shape of the electromagnetic cluster is required to be consistent with that of an electron. Also at level 3, a p_T cut of 20 to 30 GeV is applied. The efficiency is $(99.0 \pm 0.3)\%$ per electron for particles with transverse momentum $p_T > 30$ GeV and $|\eta_D| < 2$.

From events that pass these trigger requirements, dielectron candidates are selected by requiring two isolated electromagnetic clusters which have shower shapes consistent with those of electrons. The shower shape is determined by constructing a likelihood from a number of variables, such as the fraction of energy deposited in each layer of the EM portion of the calorimeter, the energy of the cluster, the vertex position, and the area of the cluster at the finely segmented third floor of the EM calorimeter. Corrections are applied to the electron energy to account for instrumental effects such as nonuniformities in the geometry of the detector and nonlinearities and gain calibrations in the readout electronics. A candidate cluster is considered to be isolated when the ratio between the energy in a cone of 0.2 in $\eta - \phi$ space to energy in a 0.4 cone is greater than 85%. Also, more than 90% of the cluster's measured energy must be in the electromagnetic portion of the calorimeter rather than in the hadron sections. Clusters which pass these criteria are considered electron candidates. One electron must have a reconstructed $p_T > 15$ GeV while the other electron has $p_T > 25$ GeV. Electrons are defined to be in the CC (EC) region of the calorimeter if they are within $|\eta_D| < 0.9$ ($1.5 < |\eta_D| < 3.2$). In the CC region, electrons are not used if they are near EM calorimeter module boundaries. As mentioned previously, at least one of the electrons in each dielectron pair must be spatially matched to a reconstructed track. In addition, all CC-region electrons are required to have a track match, so that both legs of a CC-CC event have a track match. A total of 19 306 events pass these selection criteria.

III. EFFICIENCIES AND BACKGROUNDS

Single electron efficiencies are measured from this data sample using a "tag-and-probe method." This method involves selecting a sample of $Z \rightarrow e^+e^-$ candidate events by applying tight selection criteria to one of the electron candidates, the "tag leg," and very loose selection criteria to the other electron candidate, "the probe leg." The reconstructed mass of the tag-and-probe pair are required to be close to that of a Z boson. The tag leg has tighter cuts to reduce the amount of background and to increase the probability that the event is really a boson decay event, and not from jets that are misidentified as electrons. The probe leg has looser cuts and is used to test the selection cut in question. While the efficiencies are measured with data, Monte Carlo events are used to test for biases in the efficiency measurements. For this purpose, Z/γ^* Monte Carlo events are generated with PYTHIA [10] and are processed with a full D0 detector simulation based on the GEANT software package [11], which models the interactions of particles with matter. Efficiencies are measured for identification of particles like photons and electrons that shower in the electromagnetic calorimeter ("EM particles"), shower shape cuts, trigger, and track-matching probability. All efficiencies are studied as a function of the η_D of the probe electron. In addition, some of the efficiencies are significantly dependent on additional quantities such as p_T of the probe, vertex z position of the event, boson y, or run number. The distributions of these efficiencies are parametrized using these additional quantities as necessary. Single electron efficiencies are relatively flat in η_D for the CC region, and the values are typically larger than 90%. In the EC region, the efficiencies are sensitive to changes in the calorimeter geometry, to the finite coverage of the tracking system, and to the shape of the distribution of event vertices. Because of this sensitivity, effects of

variations in the width and distribution of the vertex z distribution over the course of Run II are taken into account using a representative set of vertex distributions.

For the acceptance determination, we use the RESBOS Monte Carlo event generator [12] with CTEQ6.1M input PDFs [13,14]. RESBOS computes the differential cross section including NLO QCD corrections and uses resummation for the low p_T region. The simulated events are then processed with PHOTOS [15] to account for QED final state radiation (FSR). The events are then passed through a parametrized detector simulation which has been tuned to our data set. To properly apply efficiencies in the Monte Carlo, events are weighted based on the relative integrated luminosity per run. Figure 1 compares data to the Monte Carlo simulation; the simulated signal plus background reproduces the data well. The $\epsilon \times A$ per rapidity bin is summarized in Table I. Different vertex distributions along the beam axis are used prior to applying the efficiencies and kinematic cuts. These take into account changes in the beam z distribution over the course of our data set.

The main source of background arises from events with jets where one or more of the jets are misidentified as an electron. This category of background includes events containing a single real electron, such as $W \rightarrow e\nu$ events with associated jets. The size of the background is less than 0.8% for events where both electrons are detected in the central calorimeter (CC-CC) and less than 6% for the remainder of the data set. The background for CC-CC events is significantly smaller due to the track-match requirement on both electrons. The jet background is subtracted by fitting the di-lepton mass distribution with the sum of background and signal shapes. The signal shapes are taken from the same tuned Monte Carlo as used for the acceptance. Two different methods are used to determine the background invariant mass shape from the data. One is obtained from electron-positron events that fail the shower shape cuts; the other parametrizes the background invariant mass shape as an exponential curve and incorporates it directly into the fit of the di-electron mass distribution. The exponential fits result in about 13% more background and the average from two methods is used as the jet background contribution. In both methods, the fit is performed using only the sidebands ($40\ \text{GeV} < M_{ee} < 71\ \text{GeV}$ and $111\ \text{GeV} < M_{ee} < 130\ \text{GeV}$).

For $|y| < 2$, the jet background determination is performed separately for each rapidity bin, using the invariant mass distribution for the bin. The small numbers of events in the areas of larger $|y|$ do not permit the background fits to be performed on a bin-by-bin basis. Instead, the total background fits are performed for the entire low statistics regions of $y > 2$ and $y < -2$ separately. In each of these regions the background fraction is determined separately for three subsets of the data: CC-CC, CC-EC, and EC-EC events. The background per bin is then determined using

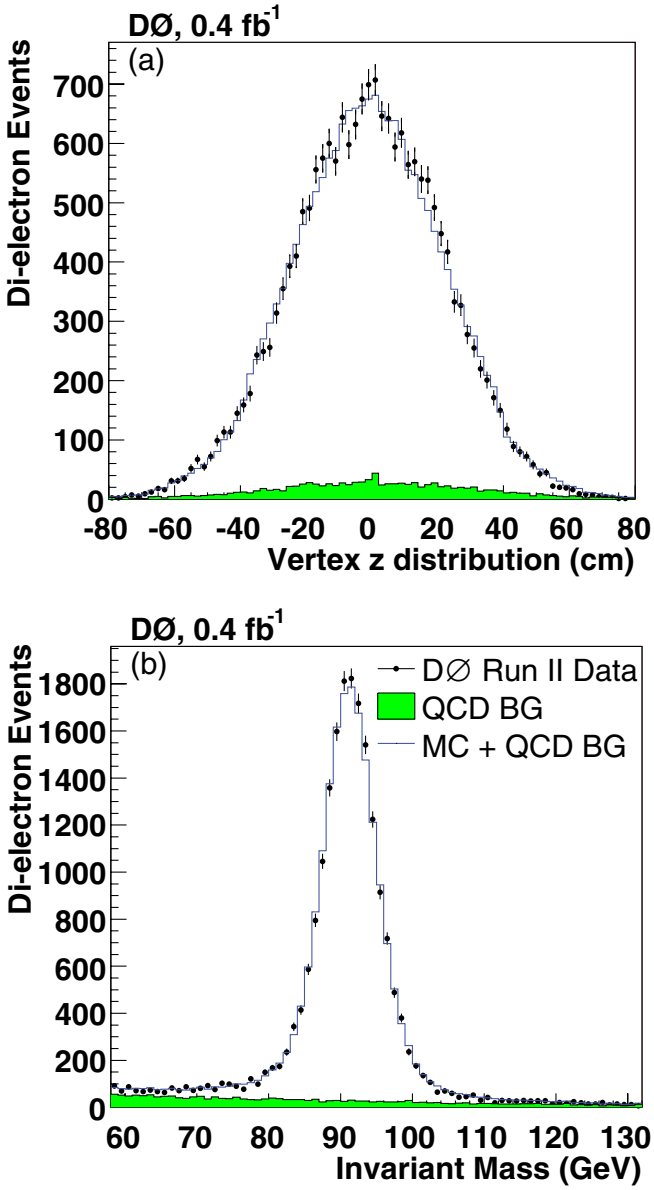

FIG. 1 (color online). Comparisons of data and Monte Carlo plus background are presented for (a) the vertex z distribution and (b) the electron-positron invariant mass spectrum. The vertex z plot shows data after all selection cuts. The data in the mass plot pass all selection criteria except for the mass cut. Uncertainties shown on the data points are statistical.

the number of candidate events collected in a given bin and the average background fraction for an appropriate subset.

Additional background contributions that could have di-lepton mass distributions could come from events that produce two real electrons or photons in the final state. To evaluate the contribution of such events, we simulate diboson events containing a W plus a W, Z, or γ; $t\bar{t}$; and $Z/\gamma^* \rightarrow \tau\tau$ events where each τ decays to an electron. All background samples are generated using PYTHIA, except for the $W + \gamma$ sample which is simulated using an event generator by Baur and Berger [16]. The combined contri-

TABLE I. Summary of the measurement of $\frac{1}{\sigma}\frac{d\sigma}{dy}$ per rapidity bin for $Z/\gamma^* \rightarrow e^+e^-$ events with mass $71 < M_{ee} < 111$ GeV.

$\lvert y\rvert$	$\frac{1}{N}\times\frac{dN}{dy} \pm$ stat. $\pm$ syst.	Candidate events	Background events	$\epsilon \times A$
0.05	$0.271 \pm 0.009\,^{+0.006}_{-0.005}$	961	21.8 ± 2.5	$0.176\,^{+0.005}_{-0.006}$
0.15	$0.276 \pm 0.009\,^{+0.007}_{-0.006}$	961	28.1 ± 3.3	$0.172\,^{+0.005}_{-0.006}$
0.25	$0.274 \pm 0.009\,^{+0.005}_{-0.005}$	924	29.0 ± 2.1	$0.166\,^{+0.004}_{-0.004}$
0.35	$0.266 \pm 0.010\,^{+0.006}_{-0.005}$	879	33.7 ± 2.8	$0.161\,^{+0.004}_{-0.005}$
0.45	$0.278 \pm 0.010\,^{+0.007}_{-0.006}$	898	37.5 ± 3.7	$0.158\,^{+0.004}_{-0.004}$
0.55	$0.269 \pm 0.010\,^{+0.006}_{-0.007}$	870	50.6 ± 3.5	$0.155\,^{+0.005}_{-0.003}$
0.65	$0.260 \pm 0.010\,^{+0.006}_{-0.006}$	882	71.3 ± 3.7	$0.159\,^{+0.004}_{-0.004}$
0.75	$0.276 \pm 0.010\,^{+0.007}_{-0.005}$	967	74.4 ± 4.2	$0.164\,^{+0.003}_{-0.005}$
0.85	$0.235 \pm 0.009\,^{+0.006}_{-0.007}$	895	88.9 ± 5.6	$0.175\,^{+0.005}_{-0.004}$
0.95	$0.244 \pm 0.009\,^{+0.005}_{-0.006}$	988	79.0 ± 5.4	$0.190\,^{+0.005}_{-0.004}$
1.05	$0.251 \pm 0.008\,^{+0.006}_{-0.006}$	1095	75.2 ± 3.8	$0.207\,^{+0.005}_{-0.006}$
1.15	$0.235 \pm 0.008\,^{+0.007}_{-0.006}$	1106	98.0 ± 8.2	$0.218\,^{+0.005}_{-0.007}$
1.25	$0.230 \pm 0.008\,^{+0.005}_{-0.006}$	1060	83.7 ± 5.5	$0.216\,^{+0.006}_{-0.005}$
1.35	$0.223 \pm 0.008\,^{+0.005}_{-0.006}$	965	94.6 ± 4.3	$0.199\,^{+0.006}_{-0.005}$
1.45	$0.211 \pm 0.008\,^{+0.004}_{-0.005}$	793	60.0 ± 2.4	$0.177\,^{+0.006}_{-0.003}$
1.55	$0.191 \pm 0.008\,^{+0.005}_{-0.006}$	694	69.5 ± 5.4	$0.167\,^{+0.005}_{-0.004}$
1.65	$0.170 \pm 0.008\,^{+0.005}_{-0.005}$	644	72.4 ± 5.1	$0.171\,^{+0.006}_{-0.005}$
1.75	$0.168 \pm 0.008\,^{+0.006}_{-0.006}$	689	79.5 ± 6.3	$0.185\,^{+0.005}_{-0.006}$
1.85	$0.142 \pm 0.007\,^{+0.005}_{-0.004}$	614	57.3 ± 5.4	$0.200\,^{+0.005}_{-0.007}$
1.95	$0.119 \pm 0.006\,^{+0.004}_{-0.004}$	559	55.5 ± 3.9	$0.216\,^{+0.006}_{-0.006}$
2.05	$0.117 \pm 0.006\,^{+0.005}_{-0.004}$	551	37.3 ± 5.7	$0.223\,^{+0.007}_{-0.009}$
2.15	$0.091 \pm 0.005\,^{+0.004}_{-0.004}$	459	36.4 ± 5.6	$0.235\,^{+0.010}_{-0.007}$
2.25	$0.069 \pm 0.004\,^{+0.003}_{-0.004}$	352	33.2 ± 5.7	$0.236\,^{+0.011}_{-0.008}$
2.35	$0.049 \pm 0.004\,^{+0.002}_{-0.002}$	232	15.4 ± 2.1	$0.224\,^{+0.012}_{-0.008}$
2.45	$0.039 \pm 0.003\,^{+0.002}_{-0.002}$	162	10.4 ± 1.1	$0.199\,^{+0.010}_{-0.012}$
2.55	$0.018 \pm 0.003\,^{+0.001}_{-0.001}$	61	3.9 ± 0.4	$0.162\,^{+0.008}_{-0.011}$
2.65	$0.014 \pm 0.003\,^{+0.001}_{-0.001}$	35	2.2 ± 0.2	$0.123\,^{+0.008}_{-0.012}$
2.75	$0.005 \pm 0.002\,^{+0.004}_{-0.004}$	10	0.6 ± 0.1	$0.085\,^{+0.009}_{-0.008}$

bution from these additional sources is insignificant compared to the background from jets. The total number of background events per bin is presented in Table I.

IV. SYSTEMATIC UNCERTAINTIES

A number of contributions to the systematic uncertainty are considered. These include contributions that arise from the determination of the $\epsilon \times A$ correction and from the measurement of the background.

As described above, two different background shapes are used to fit the di-lepton invariant mass distributions and to determine the number of background events in each $|y|$ bin. The average from the two methods is used as the background central value and the difference is split and assigned as a systematic uncertainty. An additional contribution to the background systematic uncertainty is derived by varying the constraints on the signal amplitude used in the background fits and redetermining the background.

The uncertainty on the differential cross section from the uncertainties on background ranges from 1.5%–2.0% for $|y| > 0.8$. In this region the data mainly come from the CC-EC and EC-EC configurations which, because only one track-match is required, tends to allow more background. For $|y| < 0.8$, which is dominated by CC-CC data, the uncertainty due to the background is less than 1%.

Several contributions due to the $\epsilon \times A$ measurement are taken into account. These include the uncertainties on single electron efficiencies, the electron energy scale and energy resolution, the PDFs, and the model of the vertex z distribution.

For single electron efficiencies, there are several contributions to the systematic uncertainty. Two of these contributions are derived from data while the third is obtained using Monte Carlo events. Since efficiencies are measured using data, the size of our Z/γ^* sample inherently has a limited precision. This statistical uncertainty is included as part of the systematic uncertainty. Another component of the efficiencies' systematic uncertainty comes from the background subtraction. To estimate this contribution, selection cuts are tightened on the tag electron to reduce the background at the expense of statistical precision. A comparison of the efficiencies with nominal and tighter cuts is used to estimate the systematic uncertainty from the background subtraction technique. Lastly, the tag-and-probe method used in the efficiency measurement may produce

a biased result if the efficiency for the probe electron passing the selection criteria is correlated with that of the tag electron. We estimate the size of this bias with the PYTHIA Monte Carlo sample mentioned above, which includes a full detector simulation. Efficiencies measured using generator level information about the true particle identities are compared to the same efficiencies measured via tag and probe. The difference is used as a contribution to the systematic uncertainty.

For the parametrized detector simulation, the energy response and resolutions are tuned using the width and peak position of the electron-positron mass distribution from the data sample. Kinematic variables that are correlated with the boson rapidity are not used to tune the detector simulation parameters. Changing the tuning method leads to slight variations in the energy scale and resolution parameters. From these variations, we estimate the contribution due to uncertainties on the electron energy scale. The boson rapidity measurement is not sensitive to the energy resolution.

CTEQ6.1M PDFs are defined by 20 orthogonal parameters. Each parameter has an uncertainty which is shifted separately in the positive and negative direction to provide a set of 40 PDFs for determination of the uncertainty. The acceptance is reevaluated with each PDF. Following the prescription presented in Ref. [14], we compare each acceptance to that obtained with the nominal PDF set. The differences are combined into a PDF uncertainty, with a distinction made for sets that increase or decrease the acceptance.

As mentioned above, the shape of the vertex z distribution varies with time. The width of the distribution can depend on a number of factors. The beam tuning has changed this width over the course of Run II. Also, the time elapsed since beam injection can affect the width. Since the probability of an electron to have a track-match depends in part on the z position of the primary vertex, knowledge of the vertex distribution can directly affect the acceptance correction. Samples of vertex z distributions extracted from the data in blocks corresponding to different instantaneous luminosities are used to model the vertex distribution in the Monte Carlo simulation. Selection criteria that produce the widest and narrowest vertex distribution widths are used to estimate the systematic uncertainty.

The main contributions to the total systematic uncertainty depend on the boson rapidity. At small values of $|y|$, the main sources are the single electron efficiencies ($\approx$ 2%) and the vertex z distribution ($< 1\%$). For mid-range $|y|$, the largest contributions are due to the electron efficiencies and the background subtraction. The size of each is roughly 2%. In the high rapidity region, $|y| > 2$, the main sources are from the electron efficiencies, the background, and the PDFs. The combined uncertainty in this region ranges from 3% to 10% and increases with $|y|$. The relative

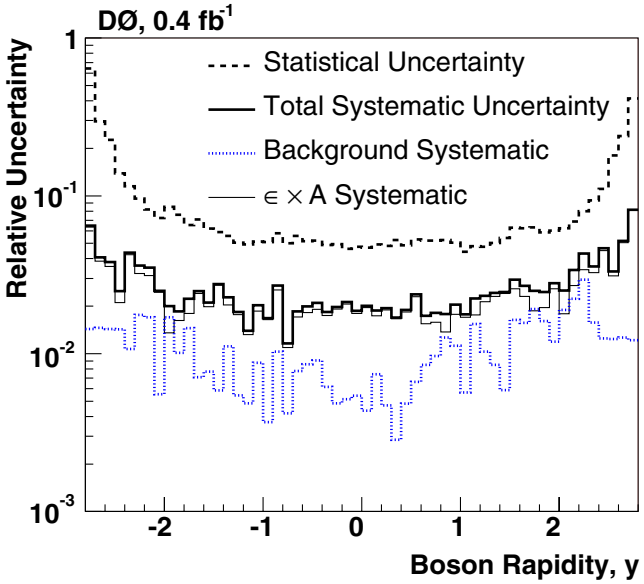

FIG. 2 (color online). Relative uncertainties plotted against the boson rapidity.

total systematic uncertainty along with the contributions to the uncertainties from the background and the $\epsilon \times A$ are presented in Fig. 2. Contributions to the $\epsilon \times A$ uncertainty also are presented for each rapidity bin in Table II.

To cross check our result, we split the data into independent sets based on criteria that should not affect the result. These include dividing the data based upon (a) time period for data collection, (b) different ranges of instantaneous luminosity, and (c) the calorimeter region in which the electrons are detected. Cross sections from independent subsets are compared to look for inconsistencies. Subsets in (a) are sensitive to hardware changes over the course of the data set and/or changes to the trigger menu used in collecting the data. Subsets in (b) have different vertex z distributions and will not agree if the vertex distribution is modeled poorly. Subsets in group (c) compare data from three separate calorimeters. All of the cross checks give results that are consistent within uncertainties.

V. RESULTS

A plot of $\frac{1}{\sigma} d\sigma/dy$ is given in Fig. 3 for Z/γ^* events within a mass range of $71 < M_{ee} < 111$ GeV. The inner (outer) error bars show the statistical (total) uncertainty. In Fig. 4 the result is shown vs $|y|$. For bin centering we follow the prescription given in Ref. [17]. The center of the bin is located at the average value of the expected distribution over the bin. For this purpose we use the NNLO calculation generated from code made available from Ref. [1]. This is a small effect and for the two decimal places of precision used here, the procedure gives the same result as using the bin center. Because of the finite resolution of the D0 detector, some fraction of the events in a given rapidity bin originates from a neighboring bin. For

TABLE II. Contributions to the systematic uncertainty for $\epsilon \times A$ are shown in bins of $|y|$. Details of the contributions are described in the text.

$\lvert y\rvert$	$\epsilon \times A$	δ (total)	δ (e^- eff.) stat.	δ (e^- eff.) method	δ (PDF)	δ (E scale)	δ (vtx z)
0.05	0.176	$^{+0.005}_{-0.006}$	± 0.0004	$^{+0.004}_{-0.004}$	$^{+0.002}_{-0.002}$	$^{+0.0009}_{-0.0002}$	$^{+0.0016}_{-0.0034}$
0.15	0.172	$^{+0.005}_{-0.006}$	± 0.0004	$^{+0.004}_{-0.004}$	$^{+0.002}_{-0.002}$	$^{+0.0010}_{-0.0006}$	$^{+0.0015}_{-0.0033}$
0.25	0.166	$^{+0.004}_{-0.004}$	± 0.0004	$^{+0.004}_{-0.004}$	$^{+0.002}_{-0.001}$	$^{+0.0007}_{-0.0011}$	$^{+0.0012}_{-0.0018}$
0.35	0.161	$^{+0.004}_{-0.005}$	± 0.0004	$^{+0.003}_{-0.004}$	$^{+0.002}_{-0.003}$	$^{+0.0002}_{-0.0004}$	$^{+0.0012}_{-0.0017}$
0.45	0.158	$^{+0.004}_{-0.004}$	± 0.0004	$^{+0.003}_{-0.003}$	$^{+0.002}_{-0.003}$	$^{+0.0006}_{-0.0002}$	$^{+0.0017}_{-0.0003}$
0.55	0.155	$^{+0.005}_{-0.003}$	± 0.0004	$^{+0.003}_{-0.003}$	$^{+0.002}_{-0.002}$	$^{+0.0015}_{-0.0007}$	$^{+0.0017}_{-0.0002}$
0.65	0.159	$^{+0.004}_{-0.004}$	± 0.0004	$^{+0.003}_{-0.004}$	$^{+0.002}_{-0.002}$	$^{+0.0013}_{-0.0002}$	$^{+0.0007}_{-0.0013}$
0.75	0.164	$^{+0.003}_{-0.005}$	± 0.0004	$^{+0.003}_{-0.003}$	$^{+0.001}_{-0.003}$	$^{+0.0011}_{-0.0003}$	$^{+0.0007}_{-0.0013}$
0.85	0.175	$^{+0.005}_{-0.004}$	± 0.0004	$^{+0.003}_{-0.004}$	$^{+0.004}_{-0.001}$	$^{+0.0013}_{-0.0004}$	$^{+0.0008}_{-0.0004}$
0.95	0.190	$^{+0.005}_{-0.004}$	± 0.0004	$^{+0.003}_{-0.004}$	$^{+0.003}_{-0.001}$	$^{+0.0002}_{-0.0013}$	$^{+0.0008}_{-0.0005}$
1.05	0.207	$^{+0.005}_{-0.006}$	± 0.0004	$^{+0.004}_{-0.004}$	$^{+0.002}_{-0.003}$	$^{+0.0007}_{-0.0005}$	$^{+0.0022}_{-0.0035}$
1.15	0.218	$^{+0.005}_{-0.007}$	± 0.0004	$^{+0.003}_{-0.005}$	$^{+0.002}_{-0.003}$	$^{+0.0014}_{-0.0005}$	$^{+0.0023}_{-0.0036}$
1.25	0.216	$^{+0.006}_{-0.005}$	± 0.0004	$^{+0.004}_{-0.004}$	$^{+0.003}_{-0.001}$	$^{+0.0013}_{-0.0004}$	$^{+0.0024}_{-0.0030}$
1.35	0.199	$^{+0.006}_{-0.005}$	± 0.0004	$^{+0.004}_{-0.003}$	$^{+0.004}_{-0.002}$	$^{+0.0008}_{-0.0004}$	$^{+0.0022}_{-0.0028}$
1.45	0.177	$^{+0.006}_{-0.003}$	± 0.0004	$^{+0.005}_{-0.003}$	$^{+0.003}_{-0.002}$	$^{+0.0004}_{-0.0009}$	$^{+0.0017}_{-0.0007}$
1.55	0.167	$^{+0.005}_{-0.004}$	± 0.0004	$^{+0.005}_{-0.003}$	$^{+0.002}_{-0.002}$	$^{+0.0012}_{-0.0009}$	$^{+0.0016}_{-0.0006}$
1.65	0.171	$^{+0.006}_{-0.005}$	± 0.0005	$^{+0.004}_{-0.002}$	$^{+0.003}_{-0.002}$	$^{+0.0013}_{-0.0007}$	$^{+0.0008}_{-0.0036}$
1.75	0.185	$^{+0.005}_{-0.006}$	± 0.0005	$^{+0.003}_{-0.004}$	$^{+0.004}_{-0.002}$	$^{+0.0009}_{-0.0006}$	$^{+0.0009}_{-0.0039}$
1.85	0.200	$^{+0.005}_{-0.007}$	± 0.0006	$^{+0.002}_{-0.006}$	$^{+0.003}_{-0.003}$	$^{+0.0015}_{-0.0008}$	$^{+0.0030}_{-0.0027}$
1.95	0.216	$^{+0.006}_{-0.006}$	± 0.0006	$^{+0.004}_{-0.004}$	$^{+0.003}_{-0.004}$	$^{+0.0010}_{-0.0001}$	$^{+0.0032}_{-0.0029}$
2.05	0.223	$^{+0.007}_{-0.009}$	± 0.0008	$^{+0.004}_{-0.005}$	$^{+0.004}_{-0.006}$	$^{+0.0026}_{-0.0002}$	$^{+0.0024}_{-0.0049}$
2.15	0.235	$^{+0.010}_{-0.007}$	± 0.0009	$^{+0.006}_{-0.004}$	$^{+0.007}_{-0.003}$	$^{+0.0012}_{-0.0013}$	$^{+0.0025}_{-0.0051}$
2.25	0.236	$^{+0.011}_{-0.008}$	± 0.0010	$^{+0.008}_{-0.005}$	$^{+0.005}_{-0.004}$	$^{+0.0011}_{-0.0014}$	$^{+0.0055}_{-0.0035}$
2.35	0.224	$^{+0.012}_{-0.008}$	± 0.0013	$^{+0.008}_{-0.006}$	$^{+0.007}_{-0.003}$	$^{+0.0010}_{-0.0019}$	$^{+0.0052}_{-0.0033}$
2.45	0.199	$^{+0.010}_{-0.012}$	± 0.0017	$^{+0.004}_{-0.007}$	$^{+0.008}_{-0.010}$	$^{+0.0028}_{-0.0000}$	$^{+0.0028}_{-0.0006}$
2.55	0.162	$^{+0.008}_{-0.011}$	± 0.0016	$^{+0.005}_{-0.007}$	$^{+0.005}_{-0.007}$	$^{+0.0017}_{-0.0031}$	$^{+0.0022}_{-0.0005}$
2.65	0.123	$^{+0.008}_{-0.012}$	± 0.0015	$^{+0.004}_{-0.006}$	$^{+0.005}_{-0.008}$	$^{+0.0019}_{-0.0044}$	$^{+0.0038}_{-0.0043}$
2.75	0.085	$^{+0.009}_{-0.008}$	± 0.0015	$^{+0.002}_{-0.006}$	$^{+0.006}_{-0.005}$	$^{+0.0048}_{-0.0008}$	$^{+0.0026}_{-0.0029}$

this analysis, about 5% of the events migrate to each adjacent bin. Even though the effect is small, a migration correction is included in the $\epsilon \times A$ determination. The uncertainties in $\frac{1}{\sigma}\mathrm{d}\sigma/\mathrm{d}y$ are dominantly statistical for all measured rapidity bins.

The values for the fraction of the cross section in each rapidity bin also are listed in Table I. No information on the bin-to-bin correlations is included in the table. Since the systematic uncertainty is small compared to the statistical uncertainty, a correlation matrix is not included. The curve in Fig. 4 is a NNLO calculation from Ref. [1] generated with MRST 2004 NNLO PDFs [18]. The calculation agrees well with our data, with a χ^2/d.o.f. of 20.0/27. Our result improves upon previous measurements over the full range in y, especially in the forward region. Figure 5 shows the relative uncertainties from the most recent boson rapidity measurement [2] and from this analysis plotted vs $|y|$. For comparison purposes, Fig. 5 also includes the relative uncertainty due to PDFs for a NLO calculation of the differential cross section. This curve uses CTEQ6M uncertainty PDFs and code from Ref. [1]. The

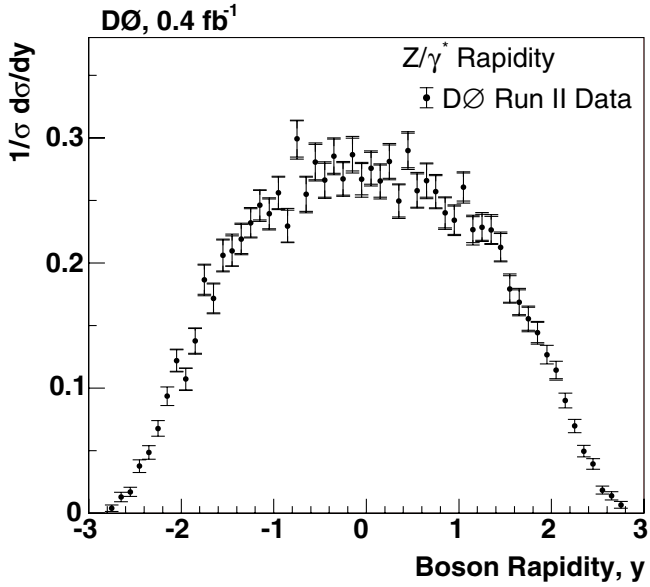

FIG. 3 (color online). D0 Run II measurement of $\frac{1}{\sigma}\mathrm{d}\sigma/\mathrm{d}y$ vs y. The inner (outer) error bars show the statistical (total) uncertainty.

method is the same as that used for the determination of the PDF uncertainty on the $\epsilon \times A$ which was discussed earlier.

In summary, we have presented a measurement of $\frac{1}{\sigma}\mathrm{d}\sigma/\mathrm{d}y$ for Z/γ^* measured with electron-positron events in the mass range $71 < M_{ee} < 111$ GeV. The measurement is the most precise measurement to date. It improves upon previous measurements and gives a significantly

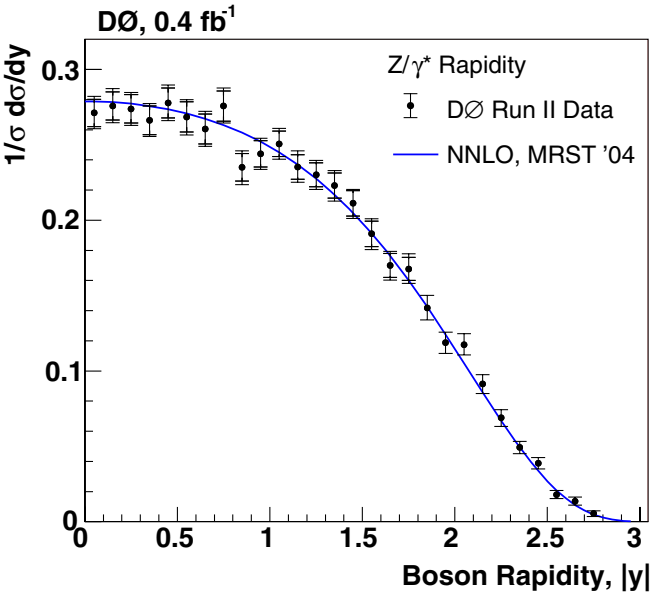

FIG. 4 (color online). D0 Run II measurement of $\frac{1}{\sigma}\mathrm{d}\sigma/\mathrm{d}y$ vs $|y|$. The inner (outer) error bars show the statistical (total) uncertainty. The curve is a NNLO calculation from [1] using MRST 2004 PDFs.

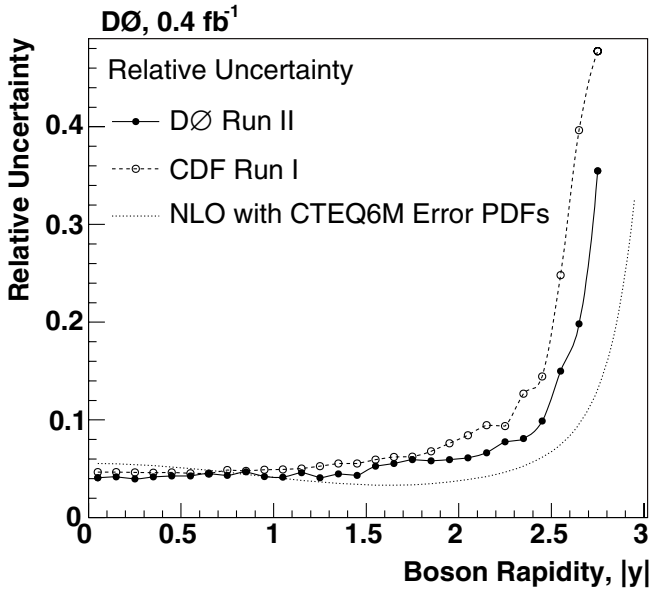

FIG. 5 (color online). Relative uncertainties from this measurement and from the CDF Run I result. Also shown is the PDF uncertainty on the differential cross section using the CTEQ6M uncertainty PDF sets. The values for the CTEQ6M curve are generated with code from Ref. [1].

more precise measurement of the boson rapidity distribution in the high rapidity region which probes the small x, high Q^2 portion of the parton distribution functions which is least constrained by other data. The fractional uncertainty in the highest rapidity bin is reduced by 30%. We find the result to be consistent with a recent NNLO calculation. The current measurement is performed with about 10% of the expected Run II integrated luminosity. An improved result is foreseen with the inclusion of additional data, which will reduce the current still-dominant statistical uncertainty.

ACKNOWLEDGMENTS

We are grateful to Csaba Balazs for his help with RESBOS. We thank the staffs at Fermilab and collaborating institutions, and acknowledge support from the DOE and NSF (USA); CEA and CNRS/IN2P3 (France); FASI, Rosatom, and RFBR (Russia); CAPES, CNPq, FAPERJ, FAPESP, and FUNDUNESP (Brazil); DAE and DST (India); Colciencias (Colombia); CONACyT (Mexico); KRF and KOSEF (Korea); CONICET and UBACyT (Argentina); FOM (The Netherlands); PPARC (United Kingdom); MSMT (Czech Republic); CRC Program, CFI, NSERC, and WestGrid Project (Canada); BMBF and DFG (Germany); SFI (Ireland); The Swedish Research Council (Sweden); Research Corporation; Alexander von Humboldt Foundation; and the Marie Curie Program.

[1] C. Anastasiou, L. Dixon, K. Melnikov, and F. Petriello, Phys. Rev. D **69**, 094008 (2004).
[2] A. A. Affolder *et al.* (CDF Collaboration), Phys. Rev. D **63**, 011101 (2000).
[3] V. N. Gribov and L. N. Lipatov, Sov. J. Nucl. Phys. **15**, 438 (1972); **15**, 675 (1972); Yu. L. Dokshitzer, Sov. Phys. JETP **46**, 641 (1977); G. Altarelli and G. Parisi, Nucl. Phys. **B126**, 298 (1977).
[4] V. Abazov *et al.* (D0 Collaboration), Nucl. Instrum. Methods Phys. Res., Sect. A **565**, 463 (2006).
[5] In this paper, electrons refers to both electrons and positrons.
[6] Vertices are determined by using the highest $\sum \log p_T^{\text{track}}$ in a two-pass algorithm. First the vertices are calculated using a loose selection criteria. For the second pass, the found vertex position and errors are used as inputs for track selection and vertex fitting.
[7] S. Abachi *et al.* (D0 Collaboration), Nucl. Instrum. Methods Phys. Res., Sect. A **338**, 185 (1994).
[8] V. M. Abazov *et al.*, Nucl. Instrum. Methods Phys. Res., Sect. A **552**, 372 (2005).
[9] D0 uses a right-handed coordinate system in which the z-axis points along the proton beam direction and the y-axis points upward. θ is the polar angle and ϕ is the azimuthal angle.
[10] T. Sjöstrand *et al.*, Comput. Phys. Commun. **135**, 238 (2001).
[11] R. Brun and F. Carminati, CERN Program Library Long Writeup W5013, 1993 (unpublished).
[12] C. Balazs and C. P. Yuan, Phys. Rev. D **56**, 5558 (1997).
[13] J. Pumplin *et al.*, J. High Energy Phys. 07 (2002) 012.
[14] D. Stump *et al.*, J. High Energy Phys. 10 (2003) 046.
[15] P. Golonka and Z. Was, Eur. Phys. J. C **45**, 97 (2006).
[16] U. Baur and E. L. Berger, Phys. Rev. D **41**, 1476 (1990).
[17] G. D. Lafferty and T. R. Wyatt, Nucl. Instrum. Methods Phys. Res., Sect. A **355**, 541 (1995).
[18] A. D. Martin, R. G. Roberts, W. J. Stirling, and R. S. Thorne, Phys. Lett. B **604**, 61 (2004).